Characterization of zero-energy corner states in higher-order topological systems with chiral symmetry

Wen-Jie Yang, Shi-Feng Li, Xin-Ye Zou,* and Jian-Chun Cheng

Key Laboratory of Modern Acoustics, MOE, Institute of Acoustics, Department of Physics, Collaborative Innovation Center of Advanced Microstructures, Nanjing University, Nanjing 210093, People's Republic of China

(Received 2 June 2023; revised 30 December 2023; accepted 5 January 2024; published 29 January 2024)

Corner-localized states represent intriguing aspects of higher-order topological systems. Despite their importance, the topological invariant that distinguishes between zero-energy and non-zero-energy corner states has received limited attention in the literature. Therefore, we introduce "modified multipole chiral numbers," utilizing the 2-norm of the pseudo wave vector to characterize zero-energy corner states and to categorize the topological phase in chiral-symmetric two-dimensional and one-dimensional systems. The quantified topological invariant, protected by chiral symmetry, is associated with the quantity and spatial distribution of the zero-energy corner states. Theoretical analyses were conducted using multiple models, and both simulations and experimental data gathered from honeycomb lattices in acoustic systems corroborate these insights. These results offer valuable guidelines for designing systems that feature topologically protected corner states across various platforms and open avenues for the exploration of boundary-obstructed topological phases.

DOI: 10.1103/PhysRevB.109.024114

I. INTRODUCTION

The discovery of higher-order topological (HOT) insulators has significantly improved our understanding of topological phases [1–18]. In a d-dimensional (dD) topological system, boundary states appear with n dimensions when the condition $d > n$ is met. Systems featuring boundary states of different dimensions are classified into distinct topological phases [19–25]. Remarkably, even when systems possess the same type of boundary states, such as zero-dimensional (0D) corner states, they can exist in disparate topological phases [26–29]. Many researchers have reported the existence of different dimensional topological states [30–54]. Although considerable focus has been directed toward understanding the origins of corner states in various studies [4–8,11,14,17], there remains a conspicuous gap in the literature concerning the direct characterization of zero-energy corner states, especially when extrinsic symmetries are not in play. Furthermore, the HOT phase of 2D honeycomb lattices has predominantly been understood within the framework of Z_2 classification [34,35,45,49]. An interplay between classical notions, such as the electric quadrupole moment, and topological invariants provides a novel avenue for further research [2,3,55–57].

In the context of crystalline solids, macroscopic polarization is not limited to structural aspects but also extends its relevance to the classification of band topology [58–60]. Approaches that incorporate the expectation value of position offer valuable insights into the subtleties of polarization [61]. The concept of the electric multipole moment has been refined to include many-body operators, sharing mathematical expressions with classical definitions [55–57,62]. Nonetheless, these challenges continue to impede progress in the field [55]. For example, recent advancements have been made in calculating multipole chiral numbers in real space [29], but the characterization of zero-energy corner states is constrained by the need for a specific lattice system (limited to the square lattice). This limitation poses a significant challenge for ongoing research.

In this paper, we introduce a real-space expression of the quadrupole moment operator utilizing the 2-norm of the pseudo wave vector, as shown in Eq. (1). We also present modified multipole chiral numbers (MMCNs) to characterize zero-energy corner states. Based on phase diagram calculations for the honeycomb lattice featuring long-range hoppings, we establish the utility and physical interpretation of this topological invariant. Importantly, this approach allows us to directly characterize the number and distribution patterns of zero-energy corner states, without being contingent upon specific crystalline symmetries. This demonstrates the Z classification of the HOT phases in honeycomb lattices. To further corroborate the utility of this topological invariant, we computed two Su-Schrieffer-Heeger (SSH)-like models. Our findings indicate that the invariant is both applicable and insensitive to the choice of the origin point. To provide further validation, we constructed an acoustic model based on a honeycomb lattice. Simulation and experimental results confirmed the presence of zero-energy corner states, as evidenced by response curves generated from acoustic measurements on three distinct samples, which is consistent with our theoretical predictions.

II. THEORY

We begin with a definition of the quadrupole moment operator. Macroscopically, the expression for the quadrupole moment can be expressed as $\int_v d^3\vec{r}'\rho r_i' r_j'$, where v and ρ

*xyzou@nju.edu.cn

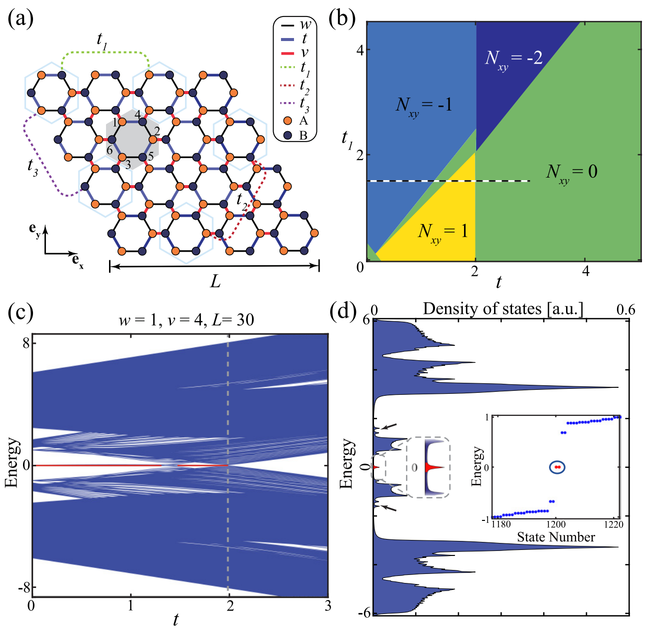

FIG. 1. (a) Diagram illustrating the honeycomb lattice incorporating long-range hopping. Light blue hexagons designate the unit cells that include long-range hopping. (b) Phase diagram displaying N_{xy} values for the honeycomb lattice where $w = 1$, and $t_3 = t_1$. (c) Energy spectra of the system with fully open boundaries, plotted as a function of t for $t_3 = t_1 = 1.5$, and $L = 30$. Dashed gray lines correspond to the right endpoint of the red line on the x axis. (d) Density of states in the system for $t = 1, t_1 = t_3 = 0$, and $L = 20$. Gray dashed rectangles highlight states with zero energy. In the corresponding subplot of energy spectra, two red dots are circumscribed by a blue circle. Parameters for both (c) and (d) are $w = 1$, $v = 4$, and $t_2 = 0$.

denote the volume of the voxel and the volume charge densities, respectively. The term $r_i' r_j'$ is the product of the position vector components of the charge within the voxel. Generalized many-body operators maintain a similar mathematical structure [55–57]. Although the intrinsic nonlinearity of these generalized operators disrupts the periodicity of the wave function, this generalization is beneficial for characterizing zero-energy corner states and their associated topological phases.

In this context, we extend the quadrupole moment operator to better suit systems exhibiting chiral symmetry. First, one can figure out the off-diagonal block Bloch Hamiltonian for the chiral-symmetric system and describe it as

$$\mathcal{H} = \begin{bmatrix} 0 & h \\ h^\dagger & 0 \end{bmatrix}.$$

In the honeycomb lattice model depicted in Fig. 1(a), the shaded hexagonal region represents the unit cell, containing six atoms labeled from 1 to 6. h can be expressed as

$$h = \begin{bmatrix} t + t_1 e^{-i2\mathbf{k}\cdot\mathbf{a}_1} & v e^{-i\mathbf{k}\cdot\mathbf{a}_3} & w \\ w & t + t_2 e^{i2\mathbf{k}\cdot\mathbf{a}_2} & v e^{i\mathbf{k}\cdot\mathbf{a}_1} \\ v e^{-i\mathbf{k}\cdot\mathbf{a}_2} & w & t + t_3 e^{i2\mathbf{k}\cdot\mathbf{a}_3} \end{bmatrix},$$

where h ($h^\dagger$) represents the sublattice A (B), with atoms 1–3 (4–6) belonging to sublattice A (B). The vectors $\mathbf{a}_i$ ($i = 1, 2, 3$) are defined as (1,0), $(1/2, \sqrt{3}/2)$, and $(1/2, -\sqrt{3}/2)$. For nearest neighbors, intracell hopping types w and t, along with intercell hopping v, are included. Long-range hopping is represented by t_1, t_2, and t_3, as illustrated by the dashed lines in Fig. 1(a). The introduced long-range hoppings are effective in demonstrating the abundant topological phase. Further details about the long-range hopping and its implications on the topological phase are available in Supplemental Material [63] Sec. I. The chiral operator is defined as $\hat{\Pi}$ $(\sigma_z \otimes \mathbb{I}_{3\times3})$, where σ_z is the Pauli matrix.

Next, the pseudo wave vector in 2D real space is defined as $\tilde{\mathbf{k}} = x/L_i\mathbf{e_x} + y/L_j\mathbf{e_y}$, where $L_{i,j}$ and (x, y) refer to the number of units along each side of the finite structure and the unit cell position within the basis $(\mathbf{e_x}, \mathbf{e_y})$, respectively. The 2-norm of $\tilde{\mathbf{k}}$ is formulated as follows,

$$\| \tilde{\mathbf{k}} \|_2 = \sqrt{\left(\frac{x}{L_i}\right)^2 + \left(\frac{y}{L_j}\right)^2}. \tag{1}$$

Compared to the product form of its components (e.g., xy/L_iL_j), the 2-norm of the pseudo wave vector in 2D polar coordinates eliminates the polar angle information which may render the quadrupole moment operator more compatible (see Supplemental Material [63] Sec. II). In 2D real space, the quadrupole moment operator of the sublattice S (either A or B) is defined by

$$Q_{xy}^S = \sum_{\mathbf{R},\alpha\in S} |\mathbf{R}, \alpha\rangle \exp(-i2\pi \| \tilde{\mathbf{k}} \|_2)\langle \mathbf{R}, \alpha|, \tag{2}$$

where $\mathbf{R}, \alpha$ denote the unit cell position in real space and the atom orbital, respectively. Upon projecting the operator Q_{xy}^S into the subspace U_S, the MMCNs can be calculated as $N_{xy} = \frac{1}{2\pi i}\mathrm{Tr}\log(\bar{\mathrm{Q}}_{xy}^A \bar{\mathrm{Q}}_{xy}^{B\dagger})$, where $\bar{\mathrm{Q}}_{xy}^S = U_S^\dagger \mathrm{Q}_{xy}^S U_S$ (with $S = A, B$), and U_S is obtained from the singular value decomposition of h ($h = U_A \Sigma U_B^\dagger$). The value of N_{xy} should be quantized under specific conditions relating to the sublattices and degrees of freedom within each unit cell [29]. Following the introduction of MMCNs, they are utilized to characterize zero-energy corner states in finite systems. Subsequently, all computational outcomes for the honeycomb lattice are based on constant parameters v (=4) and t_2 (=0). The setting for t_2 can also be changed, which has no influence to the characterization with N_{xy}. By evaluating N_{xy} as a function of t and t_1, a phase diagram is constructed, as presented in Fig. 1(b). The color-coded regions delineate different phases distinguished by their respective N_{xy} values. Examining parameter values along the striped white and black lines in Fig. 1(b) and computing the energy spectra of the finite system, it is revealed that zero-energy corner states are likely to occur when t is approximately within the interval (0, 1.25) and (1.45, 2), as marked by the red lines in Fig. 1(c). This finding corroborates the N_{xy} phase diagram. Figure 1(d) depicts the density of states, further substantiating the presence of zero-energy corner states. A subplot demonstrates the energy spectra of a finite system featuring two zero-energy corner states when $t = 1$ and in the absence of long-range hopping. The nonzero-energy corner states, which lack topological protection, are highlighted by black arrows and demonstrate a sensitivity to

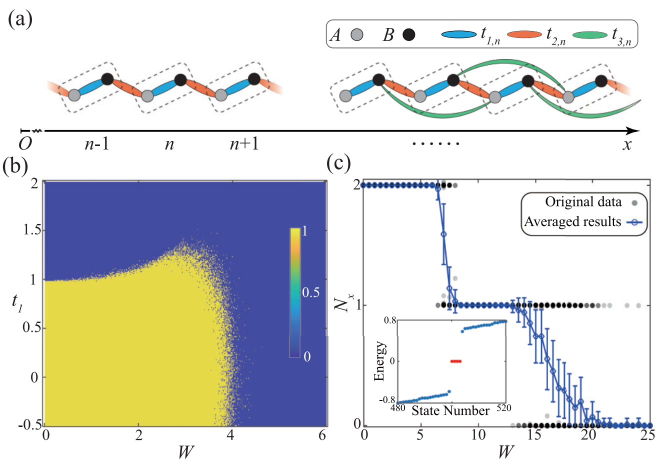

FIG. 2. (a) Diagram depicting 1D TIs based on the SSH model. Numerical labels along the x axis represent lattice indices and their spatial positions, using the lattice constant as the unit length. Gray (black) atoms in each unit cell belong to sublattice A (B). (b) Phase diagram showing N_x values for the model without long-range couplings in (a). Yellow (blue) regions correspond to N_x values of 1 (0). (c) N_x values for the model incorporating long-range couplings as a function of disorder strength W. The subplot reveals portions of the energy spectra for a system with four zero-energy corner states at $W = 2$. For this case, $t_3 = -2$, $W_3 = 0$, and $t_1 = 0$. Parameters for both (b) and (c) include $W_1 = 2W_2 = W$, $t_2 = 1$, $x_0 = 20$, and $L = 501$.

the disorder [34,35]. In addition, the difference of the two kinds of corner states can be detected based on the relevant works [34,35]. The number of zero-energy corner states is a function of N_{xy}. Specifically, if $N_{xy} = n$, then $2|n|$ zero-energy corner states exist. Furthermore, positive (negative) N_{xy} values imply the distribution of these states solely within sublattices A (B), as elaborated in Supplemental Material [63] Sec. III. Adhering to the same methodology, the norm of the pseudo wave vector in a 1D system is defined as $|\tilde{\mathbf{k}}| = |x - x_0|/L$, where L, x, and x_0 represent the total number of unit cells, the position of a particular unit cell, and the translations of the origin point, respectively. We specifically calculated the MMCNs for 1D systems, denoted as N_x, in the context of two classical SSH-like models previously explored [2,26,28]. The second-quantized Hamiltonian for the model depicted in Fig. 2(a) can be described as follows,

$$\mathcal{H} = -\sum_{n=1}^{N} (t_{1,n}\hat{a}_n^\dagger \hat{b}_n + t_{2,n}\hat{a}_{n+1}^\dagger \hat{b}_n + t_{3,n}\hat{a}_{n+2}^\dagger \hat{b}_n) + \text{H.c.}, \quad (3)$$

where $\hat{a}_n$ ($\hat{b}_n$) generates a particle in the A (B) sublattice of the nth cell. The variable $t_{i,n} = t_n + W_i \varepsilon_{i,n}$, with $i = 1, 2, 3$, denotes the hopping strength, where $\varepsilon_{i,n}$ is a uniformly distributed random strength $(-1/2, 1/2)$, and W_i signifies the disorder strength. Introducing disorder allows for the examination of the interplay between disorder and topological features, as well as the robustness of MMCNs. When the next-next-nearest-neighbor (NNNN) term $t_{3,n} = 0$, as expressed in Eq. (3), the model corresponds to the one depicted in the left panel of Fig. 2(a). Figure 2(b) presents the phase diagram of N_x as a function of disorder strength W ($W_1 = 2W_2 = W$) and intracell hopping t_1, which aligns precisely with previous results based on the winding number [2,64]. Upon the inclusion of the NNNN term, phase transitions manifest with increasing W, maintaining the quantitative relationship between MMCNs and the number of zero-energy corner states, as illustrated in Fig. 2(c). The solid blue line with circles and error bars conveys the average outcomes from 100 random realizations, while the single gray dot signifies an individual random realization. Notably, the predictive accuracy of the model improves as the finite system's size increases. Furthermore, in the case of systems that break time-reversal symmetry (classified as class AIII in the tenfold scheme), MMCNs continue to be a dependable metric for precisely characterizing the topological phase (see Supplemental Material [63] Sec. IV). It should be noted that, despite the pseudo-wave-vector norm incorporating the absolute value of the position, neither N_x nor N_{xy} is sensitive to the translation of the original point, as further explained in Supplemental Material [63] Sec. V.

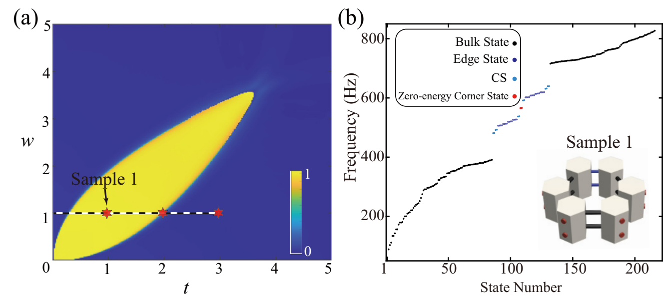

FIG. 3. (a) Phase diagram of N_{xy} for a honeycomb lattice without long-range hoppings. The three red stars denote the parameter coordinates (w, t) of (1,1), (1,2), and (1,3). The color bar signifies the magnitude of N_{xy}, with a fixed lattice size L of 20. (b) Eigenfrequencies for a finite rhombic acoustic structure. Red dots (alongside sky blue, blue, and black) signify zero-energy corner (nonzero-energy corner, edge, and bulk) states. The acoustic structure depicted in the subplot corresponds to the first red star in (a).

III. SIMULATION AND EXPERIMENT

To corroborate the theoretical findings, both simulations and experimental setups were employed using acoustic resonance systems based on a finite honeycomb lattice structure. For the sake of simplicity, all long-range hopping parameters were set to zero. The resulting phase diagram of N_{xy} as a function of w and t is shown in Fig. 3(a). It is observed that the value of N_{xy} oscillates between 0 and 1 as the parameter t is varied along with the black and white striped lines in the figure. In accordance with previous studies [65,66], we can map the hopping parameters of the theoretical model to the geometrical parameters of the acoustic structures. The eigenvalues of the Hamiltonian matrix in the theoretical model correspond to the eigenfrequencies of the acoustic structures, as detailed in Supplemental Material [63] Sec. VI.

We then measured the response curves to acoustic sources placed at varying locations—the bulk, edges, and corners—of the finite system. Three acoustic samples were engineered to mirror the corresponding theoretical models, as indi-

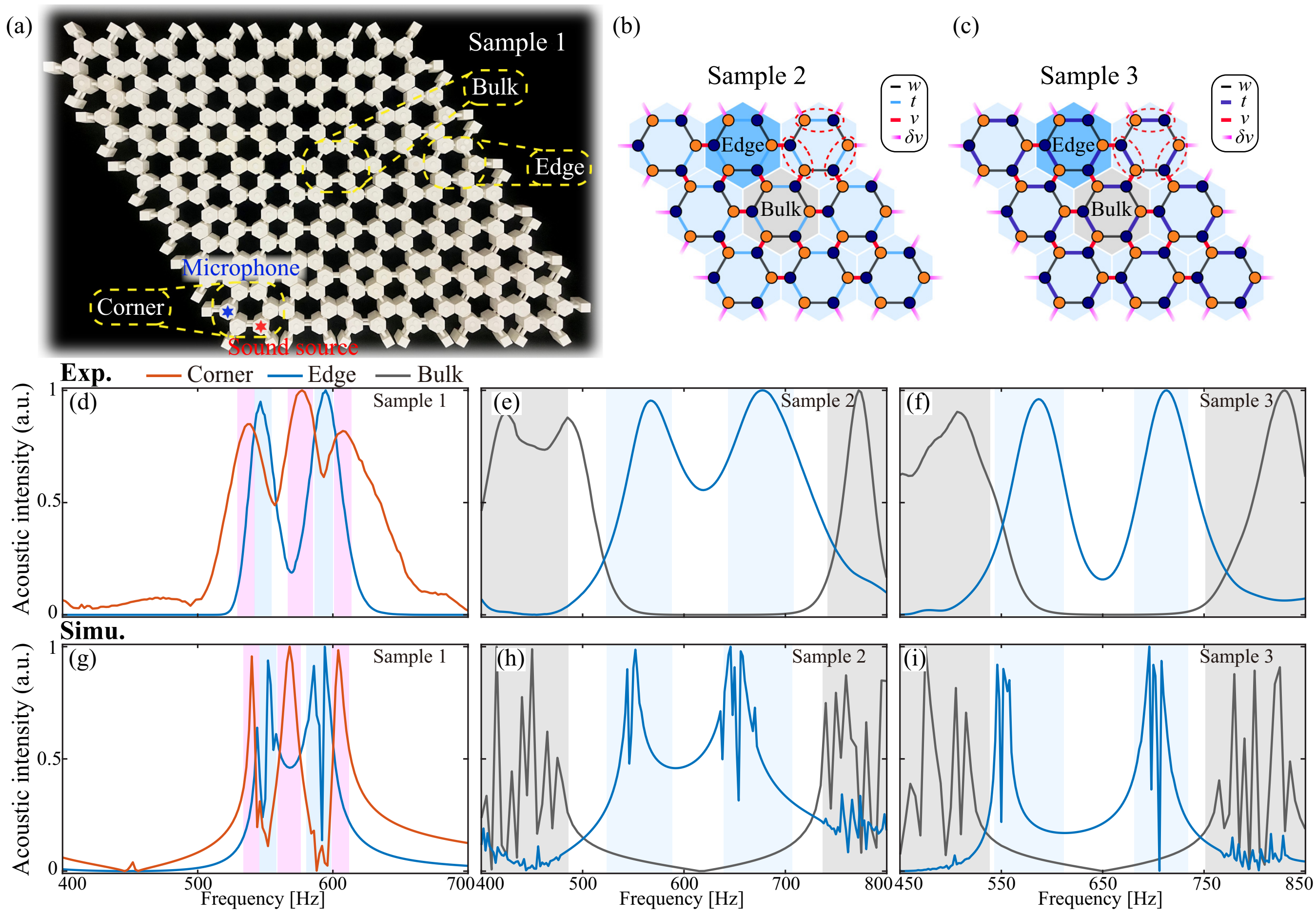

FIG. 4. Results of experiment and simulation. (a) 3D-printed structure of sample 1, highlighting test positions for corner, edge, and bulk responses. The red (blue) star marks the position of microphone (loudspeaker). (b) Schematic of sample 2, and (c) schematic diagram of sample 3. A red dashed ellipse accentuates the varying hopping strength t between the two samples. Units with dark blue and gray backgrounds pinpoint the relative test positions. (d)–(f) Measured frequency response curves pertinent to sample 1, sample 2, and sample 3. The trio of blue lines present two peaks at frequencies of (546, 594), (566, 675), and (586, 713) Hz, respectively. Orange (blue, gray) lines represent the frequency response curves at the corner (edge, bulk) positions in each sample. (g)–(i) Simulated frequency response curves for sample 1, sample 2, and sample 3. Shaded regions in (d)–(i) facilitate the identification of peak locations.

cated by the three red stars in Fig. 3(a) to substantiate the effectiveness of N_{xy} (see Supplemental Material [63] Sec. VI). Upon assembling these acoustic units into a finite rhombic configuration and determining their eigenfrequencies, it was discovered that zero-energy corner states emerge at the middle of the gap in the eigenfrequency spectra, as indicated by the red dots in Fig. 3(b). Most significantly, the presence of these zero-energy corner states serves as an emblematic feature of the system's nontrivial topological attributes. In contrast, corner states with nonzero energy, labeled as CS, do not enjoy topological protection. An analysis of the energy spectra for the trio of acoustic samples revealed that the phase transition of edge states governs the occurrence of zero-energy corner states. This is further elaborated in Supplemental Material [63] Sec. VI. Consequently, it becomes evident that MMCNs are instrumental in investigating edge-corner correspondence via the characterization of zero-energy corner states.

In the experiment, three acoustic samples were fabricated to represent the manifestation, transitional state, and absence of zero-energy corner states. Figure 4(a) depicts the 3D-printed architecture of sample 1, with yellow circles denoting the points where corner, edge, and bulk response curves were measured relative to the acoustic source. By positioning the microphone and sound source at the locations identified by blue and red stars in the corner of sample 1, the frequency response curve was ascertained, as illustrated by the orange line in Fig. 4(d). The frequency corresponding to the second peak on this curve is 576 Hz, aligning with the frequency of the zero-energy eigenvalue, as marked by red dots in Fig. 3(b). In contrast, the corners of samples 2 and 3 yielded no such discernible peaks, as elaborated in Supplemental Material [63] Sec. VII. It is worth mentioning that the nonzero-energy corner states can exist independently from the zero-energy corner states and the introduced topological invariant cannot differentiate the two kinds of corner states. Response curves for edge and bulk regions were also obtained by positioning the microphone and sound source in the designated test units. Moreover, it was observed that the peaks in these edge and bulk response curves were situated entirely within the eigenfrequency range associated with edge and bulk states, as outlined in Supplemental Material [63] Sec. VI and depicted in Figs. 4(e) and 4(f). All measurements were executed utilizing a B&K PULSE (type-4191) instrument. Simultaneously, simulations were performed to replicate the experimental procedures. The resulting simulated response curves, as displayed in Figs. 4(g)–4(i), were consistent with the measured data. To easily identify the peak positions in Figs. 4(d)–4(i), shaded regions were incorporated into the visual representation. Lastly, Helmholtz resonators were affixed to the peripheral tubes of the acoustic structure to maintain a soft boundary condition, as detailed in Supplemental Material [63] Sec. VI.

IV. CONCLUSION

In conclusion, we introduced an expression for the quadrupole moment operator aimed at characterizing zero-energy corner states, bypassing the constraints of traditional mathematical generalizations. This approach enhances the operator's compatibility with the systems under study. By computing the MMCNs for both 2D honeycomb lattice models and 1D SSH-like models featuring long-range hopping, we established that MMCNs offer a robust means of characterizing both the zero-energy corner states and their associated topological phases. Despite the seemingly counterintuitive approach of utilizing the norm of the pseudo wave vector, we found that this quantity is notably insensitive to translational adjustments of the initial point, thus rendering the quantized outcomes reliable indicators. In addition, we developed an effective acoustic model to empirically validate our theoretical constructs. Meanwhile, the MMCNs can help to demonstrate the edge-corner correspondence by characterizing the zero-energy corner states. These advancements hold significant promise for guiding the design of systems with topologically protected zero-energy corner states across diverse platforms, including topoelectric circuits and photonics, and various application fields, such as topological lasers [67].

ACKNOWLEDGMENTS

This work is supported by the National Natural Science Foundation of China (Grants No. 12074184, No. 12274219, and No. 11934009), and the Key Research and Development Project of Jiangsu Province (Grant No. BE2022814).

[1] R.-J. Slager, L. Rademaker, J. Zaanen, and L. Balents, Impurity-bound states and Green's function zeros as local signatures of topology, Phys. Rev. B **92**, 085126 (2015).

[2] W. A. Benalcazar, B. A. Bernevig, and T. L. Hughes, Electric multipole moments, topological multipole moment pumping, and chiral hinge states in crystalline insulators, Phys. Rev. B **96**, 245115 (2017).

[3] W. A. Benalcazar, B. A. Bernevig, and T. L. Hughes, Quantized electric multipole insulators, Science **357**, 61 (2017).

[4] F. Liu and K. Wakabayashi, Novel topological phase with a zero Berry curvature, Phys. Rev. Lett. **118**, 076803 (2017).

[5] Z. Song, Z. Fang, and C. Fang, $(d-2)$-dimensional edge states of rotation symmetry protected topological states, Phys. Rev. Lett. **119**, 246402 (2017).

[6] J. Langbehn, Y. Peng, L. Trifunovic, F. von Oppen, and P. W. Brouwer, Reflection-symmetric second-order topological insulators and superconductors, Phys. Rev. Lett. **119**, 246401 (2017).

[7] M. Ezawa, Higher-order topological insulators and semimetals on the breathing kagome and pyrochlore lattices, Phys. Rev. Lett. **120**, 026801 (2018).

[8] O. Pozo, C. Repellin, and A. G. Grushin, Quantization in chiral higher order topological insulators: Circular dichroism and local Chern marker, Phys. Rev. Lett. **123**, 247401 (2019).

[9] E. Khalaf, Higher-order topological insulators and superconductors protected by inversion symmetry, Phys. Rev. B **97**, 205136 (2018).

[10] M. Geier, L. Trifunovic, M. Hoskam, and P. W. Brouwer, Second-order topological insulators and superconductors with an order-two crystalline symmetry, Phys. Rev. B **97**, 205135 (2018).

[11] W. A. Benalcazar, T. Li, and T. L. Hughes, Quantization of fractional corner charge in C_n-symmetric higher-order topological crystalline insulators, Phys. Rev. B **99**, 245151 (2019).

[12] X. Zhang, H.-X. Wang, Z.-K. Lin, Y. Tian, B. Xie, M.-H. Lu, Y.-F. Chen, and J.-H. Jiang, Second-order topology and multidimensional topological transitions in sonic crystals, Nat. Phys. **15**, 582 (2019).

[13] F. Liu, H.-Y. Deng, and K. Wakabayashi, Helical topological edge states in a quadrupole phase, Phys. Rev. Lett. **122**, 086804 (2019).

[14] F. Schindler, M. Brzezińska, W. A. Benalcazar, M. Iraola, A. Bouhon, S. S. Tsirkin, M. G. Vergniory, and T. Neupert, Fractional corner charges in spin-orbit coupled crystals, Phys. Rev. Res. **1**, 033074 (2019).

[15] M. Li, D. Zhirihin, M. Gorlach, X. Ni, D. Filonov, A. Slobozhanyuk, A. Alù, and A. B. Khanikæv, Higher-order topological states in photonic kagome crystals with long-range interactions, Nat. Photonics **14**, 89 (2020).

[16] E. Khalaf, W. A. Benalcazar, T. L. Hughes, and R. Queiroz, Boundary-obstructed topological phases, Phys. Rev. Res. **3**, 013239 (2021).

[17] M. Ezawa, Edge-corner correspondence: Boundary-obstructed topological phases with chiral symmetry, Phys. Rev. B **102**, 121405(R) (2020).

[18] C. W. Peterson, T. Li, W. A. Benalcazar, T. L. Hughes, and G. Bahl, A fractional corner anomaly reveals higher-order topology, Science **368**, 1114 (2020).

[19] M. Z. Hasan and C. L. Kane, *Colloquium:* Topological insulators, Rev. Mod. Phys. **82**, 3045 (2010).

[20] X.-L. Qi and S.-C. Zhang, Topological insulators and superconductors, Rev. Mod. Phys. **83**, 1057 (2011).

[21] J. Kruthoff, J. de Boer, J. Van Wezel, C. L. Kane, and R.-J. Slager, Topological classification of crystalline insulators through band structure combinatorics, Phys. Rev. X **7**, 041069 (2017).

[22] F. Schindler, A. M. Cook, M. G. Vergniory, Z. Wang, S. S. P. Parkin, B. A. Bernevig, and T. Neupert, Higher-order topological insulators, Sci. Adv. **4**, eaat0346 (2018).

[23] E. Khalaf, H. C. Po, A. Vishwanath, and H. Watanabe, Symmetry indicators and anomalous surface states of topological crystalline insulators, Phys. Rev. X **8**, 031070 (2018).

[24] L. Trifunovic and P. W. Brouwer, Higher-order bulk-boundary correspondence for topological crystalline phases, Phys. Rev. X **9**, 011012 (2019).

[25] B. Xie, H.-X. Wang, X. Zhang, P. Zhan, J.-H. Jiang, M. Lu, and Y. Chen, Higher-order band topology, Nat. Rev. Phys. **3**, 520 (2021).

[26] J. Song and E. Prodan, AIII and BDI topological systems at strong disorder, Phys. Rev. B **89**, 224203 (2014).

[27] I. Mondragon-Shem, T. L. Hughes, J. Song, and E. Prodan, Topological criticality in the chiral-symmetric AIII class at strong disorder, Phys. Rev. Lett. **113**, 046802 (2014).

[28] L. Lin, Y. Ke, and C. Lee, Real-space representation of the winding number for a one-dimensional chiral-symmetric topological insulator, Phys. Rev. B **103**, 224208 (2021).

[29] W. A. Benalcazar and A. Cerjan, Chiral-symmetric higher-order topological phases of matter, Phys. Rev. Lett. **128**, 127601 (2022).

[30] M. Xiao, G. Ma, Z. Yang, P. Sheng, Z. Q. Zhang, and C. T. Chen, Geometric phase and band inversion in periodic acoustic systems, Nat. Phys. **11**, 240 (2015).

[31] S. Imhof, C. Berger, F. Bayer, J. Brehm, L. W. Molenkamp, T. Kiessling, F. Schindler, C. H. Lee, M. Greiter, T. Neupert, and R. Thomale, Topolectrical-circuit realization of topological corner modes, Nat. Phys. **14**, 925 (2018).

[32] M. Serra-Garcia, V. Peri, R. Süsstrunk, O. R. Bilal, T. Larsen, L. G. Villanueva, and S. D. Huber, Observation of a phononic quadrupole topological insulator, Nature (London) **555**, 342 (2018).

[33] C. W. Peterson, W. A. Benalcazar, T. L. Hughes, and G. Bahl, A quantized microwave quadrupole insulator with topologically protected corner states, Nature (London) **555**, 346 (2018).

[34] H. Fan, B. Xia, L. Tong, S. Zheng, and D. Yu, Elastic higher-order topological insulator with topologically protected corner states, Phys. Rev. Lett. **122**, 204301 (2019).

[35] X. Ni, M. Weiner, A. Alù, and A. B. Khanikaev, Observation of higher-order topological acoustic states protected by generalized chiral symmetry, Nat. Mater. **18**, 113 (2019).

[36] Z. Zhang, H. Long, C. Liu, C. Shao, Y. Cheng, X. Liu, and J. Christensen, Deep-subwavelength holey acoustic second-order topological insulators, Adv. Mater. **31**, 1904682 (2019).

[37] B.-Y. Xie, G.-X. Su, H.-F. Wang, H. Su, X.-P. Shen, P. Zhan, M.-H. Lu, Z.-L. Wang, and Y.-F. Chen, Visualization of higher-order topological insulating phases in two-dimensional dielectric photonic crystals, Phys. Rev. Lett. **122**, 233903 (2019).

[38] S. Liu, W. Gao, Q. Zhang, S. Ma, L. Zhang, C. Liu, Y. J. Xiang, T. J. Cui, and S. Zhang, Topologically protected edge state in two-dimensional Su-Schrieffer-Heeger circuit, Research **2019**, 8609875 (2019).

[39] A. El Hassan, F. K. Kunst, A. Moritz, G. Andler, E. J. Bergholtz, and M. Bourennane, Corner states of light in photonic waveguides, Nat. Photonics **13**, 697 (2019).

[40] S. Mittal, V. V. Orre, G. Zhu, M. A. Gorlach, A. Poddubny, and M. Hafezi, Photonic quadrupole topological phases, Nat. Photonics **13**, 692 (2019).

[41] H. Xue, Y. Yang, F. Gao, Y. Chong, and B. Zhang, Acoustic higher-order topological insulator on a kagome lattice, Nat. Mater. **18**, 108 (2019).

[42] M. Weiner, X. Ni, M. Li, A. Alù, and A. B. Khanikæv, Demonstration of a third-order hierarchy of topological states in a three-dimensional acoustic metamaterial, Sci. Adv. **6**, eaay4166 (2020).

[43] Y. Qi, C. Qiu, M. Xiao, H. He, M. Ke, and Z. Liu, Acoustic realization of quadrupole topological insulators, Phys. Rev. Lett. **124**, 206601 (2020).

[44] C. He, H.-S. Lai, B. He, S.-Y. Yu, X. Xu, M.-H. Lu, and Y.-F. Chen, Acoustic analogues of three-dimensional topological insulators, Nat. Commun. **11**, 2318 (2020).

[45] Z.-X. Li, Y. Cao, X. R. Wang, and P. Yan, Symmetry-protected zero modes in metamaterials based on topological spin texture, Phys. Rev. Appl. **13**, 064058 (2020).

[46] X. Ni, M. Li, M. Weiner, A. Alù, and A. B. Khanikaev, Demonstration of a quantized acoustic octupole topological insulator, Nat. Commun. **11**, 2108 (2020).

[47] M. Proctor, P. A. Huidobro, B. Bradlyn, M. B. De Paz, M. G. Vergniory, D. Bercioux, and A. García-Etxarri, Robustness of topological corner modes in photonic crystals, Phys. Rev. Res. **2**, 042038(R) (2020).

[48] A.-Y. Guan, Z.-Z. Yang, W.-J. Yang, X.-Y. Zou, and J.-C. Cheng, Classical Majorana-like zero modes in an acoustic Kitaev chain, Phys. Rev. B **107**, 134107 (2023).

[49] W. Zhang, D. Zou, Q. Pei, W. He, J. Bao, H. Sun, and X. Zhang, Experimental observation of higher-order topological Anderson insulators, Phys. Rev. Lett. **126**, 146802 (2021).

[50] Z.-G. Chen, W. Zhu, Y. Tan, L. Wang, and G. Ma, Acoustic realization of a four-dimensional higher-order Chern insulator and boundary-modes engineering, Phys. Rev. X **11**, 011016 (2021).

[51] H. Qiu, M. Xiao, F. Zhang, and C. Qiu, Higher-order Dirac sonic crystals, Phys. Rev. Lett. **127**, 146601 (2021).

[52] Z.-G. Geng, Y.-G. Peng, H. Lv, Z. Xiong, Z. Chen, and X.-F. Zhu, Square-root-like higher-order topological states in three-dimensional sonic crystals, J. Phys.: Condens. Matter **34**, 104001 (2022).

[53] W.-J. Yang, Z.-Z. Yang, X.-Y. Zou, and J.-C. Cheng, Characterization and experimental demonstration of corner states of boundary-obstructed topological insulators in honeycomb lattice, Phys. Rev. B **107**, 174101 (2023).

[54] A.-Y. Guan, Z.-Z. Yang, W.-J. Yang, S.-F. Li, X.-Y. Zou, and J.-C. Cheng, Controlling sound wave propagation in topological crystalline insulators and rainbow-trapping, Phys. Rev. Appl. **18**, 044054 (2022).

[55] S. Ono, L. Trifunovic, and H. Watanabe, Difficulties in operator-based formulation of the bulk quadrupole moment, Phys. Rev. B **100**, 245133 (2019).

[56] B. Kang, K. Shiozaki, and G. Y. Cho, Many-body order parameters for multipoles in solids, Phys. Rev. B **100**, 245134 (2019).

[57] W. A. Wheeler, L. K. Wagner, and T. L. Hughes, Many-body electric multipole operators in extended systems, Phys. Rev. B **100**, 245135 (2019).

[58] R. D. King-Smith and D. Vanderbilt, Theory of polarization of crystalline solids, Phys. Rev. B **47**, 1651(R) (1993).

[59] D. Vanderbilt and R. D. King-Smith, Electric polarization as a bulk quantity and its relation to surface charge, Phys. Rev. B **48**, 4442 (1993).

[60] R. Resta, Macroscopic polarization in crystalline dielectrics: The geometric phase approach, Rev. Mod. Phys. **66**, 899 (1994).

[61] R. Resta, Quantum-mechanical position operator in extended systems, Phys. Rev. Lett. **80**, 1800 (1998).

[62] R. Resta and D. Vanderbilt, Theory of polarization: A modern approach, in *Physics of Ferroelectrics: A Modern Perspective* (Springer, Berlin, 2007), pp. 31–68.

[63] See Supplemental Material at http://link.aps.org/supplemental/10.1103/PhysRevB.109.024114 for more details on the application in the quadrupole topological insulators, the topological phase indicated by N_{xy}, phase diagram of the 1D model, insensitivity to the position of the original point, and the construction and the band topology of the acoustic model, which includes Ref. [2].

[64] E. J. Meier, F. A. An, A. Dauphin, M. Maffei, P. Massignan, T. L. Hughes, and B. Gadway, Observation of the topological Anderson insulator in disordered atomic wires, Science **362**, 929 (2018).

[65] A.-Y. Guan, Z.-Z. Yang, X.-Y. Zou, and J.-C. Cheng, Method to derive the Hamiltonian of acoustic topological crystalline insulators, Phys. Rev. Appl. **15**, 064056 (2021).

[66] Z.-Z. Yang, A.-Y. Guan, W.-J. Yang, X.-Y. Zou, and J.-C. Cheng, Surface impedance and generalized chiral symmetry in acoustic higher-order topological insulators, Phys. Rev. B **103**, 214112 (2021).

[67] W. Zhang, X. Xie, H. Hao, J. Dang, S. Xiao, S. Shi, H. Ni, Z. Niu, C. Wang, K. Jin *et al.*, Low-threshold topological nanolasers based on the second-order corner state, Light: Sci. Appl. **9**, 109 (2020).